IOPscience iopscience.iop.org

Home Search Collections Journals About Contact us My IOPscience

Crystal-field interactions in the pseudo-ternary compound $ErAl_xGa_{2-x}$ studied by inelastic neutron scattering

This article has been downloaded from IOPscience. Please scroll down to see the full text article.

2001 J. Phys.: Condens. Matter 13 6773

(http://iopscience.iop.org/0953-8984/13/31/314)

View the table of contents for this issue, or go to the journal homepage for more

Download details:
IP Address: 171.66.16.226
The article was downloaded on 16/05/2010 at 14:03

Please note that terms and conditions apply.

INSTITUTE OF PHYSICS PUBLISHING JOURNAL OF PHYSICS: CONDENSED MATTER

J. Phys.: Condens. Matter **13** (2001) 6773–6785 PII: S0953-8984(01)25084-X

Crystal-field interactions in the pseudo-ternary compound $ErAl_xGa_{2-x}$ studied by inelastic neutron scattering

Thierry Strässle[1], **Felix Altorfer and Albert Furrer**

Laboratory for Neutron Scattering, ETH Zürich and Paul Scherrer Institute, 5232 Villigen PSI, Switzerland

E-mail: thierry.straessle@psi.ch

Received 21 May 2001, in final form 18 June 2001
Published 19 July 2001
Online at stacks.iop.org/JPhysCM/13/6773

Abstract

The crystal field of the pseudo-ternary compound $ErAl_xGa_{2-x}$ has been determined by means of inelastic neutron scattering for $x = 0.5$, 1.0 and 1.75. The thermodynamic properties reconstructed from the obtained crystal-field parameters are compared to neutron diffraction, specific heat and magnetic susceptibility measurements. The effect of increasing the Ga concentration on the crystal-field potential with respect to the change in geometry and the electronic properties of the solid is discussed by means of an extended point-charge model. It is concluded that Ga leads to an increase of the electron concentration and thus most likely triggers the structural phase transitions in the RAl_xGa_{2-x} systems (R = rare earth) by a Hume–Rothery-like electronic mechanism. The experimentally observed large broadening of the crystal-field transitions is discussed within the framework of concentration inhomogeneities.

1. Introduction

The intermetallic compounds RAl_xGa_{2-x} show a wide variety of chemical and magnetic structures. The binary compounds RAl_2 (R = Ce, Pr, Nd, Sm, Tb, Gd, Dy, Ho, Er, Tm, Yb), i.e. $x = 2$ all crystallize in the cubic $MgCu_2$ Laves phase (space group $Fd\bar{3}m$) and exhibit ferromagnetic order (except for R = Ce) with Curie temperatures between $T_C = 5.4$ K ($TmAl_2$) and $T_C = 120$ K ($SmAl_2$) [1]. In these compounds the crystal-field parameters have been determined by various authors ([1–3] and references therein). Upon partial substitution of the Al ions by Ga many of these pseudo-ternary compounds (e.g. R = Ce, Sm, Gd, Tb, Dy, Ho, Er, Tm, Yb) realize a hexagonal AlB_2 phase (space group $P6/mmm$) and eventually another closely related structure for $x \ll 1$ [4–8]. The magnetic structure of a few of these

[1] To whom correspondence should be addressed.

 © 2001 IOP Publishing Ltd Printed in the UK

systems has been studied in detail, e.g. for R = Nd, Er [9] and Ho [6, 10]. These compounds show a large variety of frustrated magnetic arrangements in a most simple hexagonal structure. To our knowledge $NdAl_xGa_{2-x}$ [11] and HoAlGa [10] represent the only systems for which attempts at determining the crystal field (CEF) have been made so far. In the latter case, the CEF parameters, the exchange parameters and the magnetic periodicity at T_N lead to a quantitative understanding of the complex magnetic phase diagram of HoAlGa [10].

The chemical phase diagram of $ErAl_xGa_{2-x}$ is summarized in figure 1. For $x \gtrsim 1.5$ the compound remains in the cubic $MgCu_2$ structure, whereas for $x \lesssim 1.5$ the hexagonal AlB_2 structure is realized. It has been found that the AlB_2 structure generally exists in two distinct modifications with different lattice ratios c/a [4, 12–14]. For $1.5 \gtrsim x \gtrsim 0.6$ the *low-c/a* type is realized, whereas for higher Ga content the *intermediate-c/a* type becomes favoured. All pure phases are flanked by large regions of phase coexistence. The structural and magnetic properties for $x = 2$, 1.75, 1.0 and 0.5 are listed in table 1.

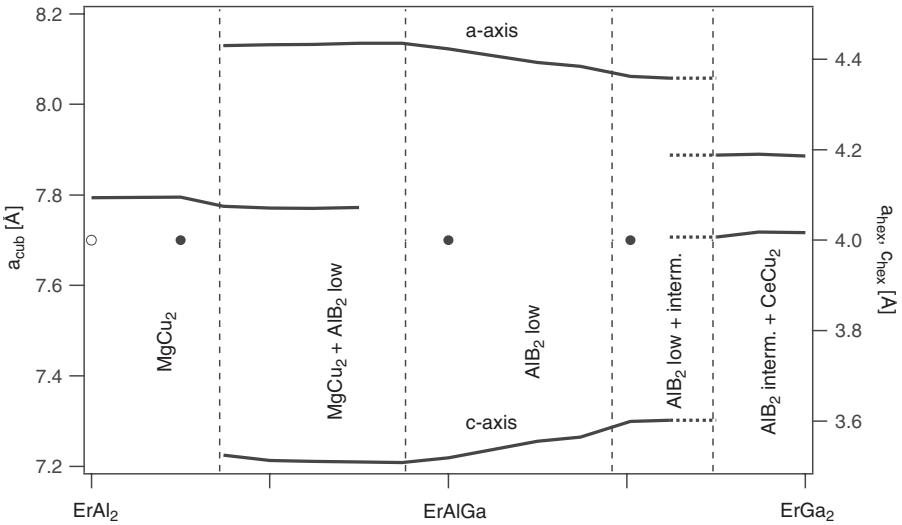

Figure 1. Phase diagram and lattice constants of $ErAl_xGa_{2-x}$ at room temperature after Martin and Girgis [5]. Markers refer to measured CEF spectra ($ErAl_2$ by Purwins and Leson [1]).

Table 1. Structural and magnetic properties of the $ErAl_xGa_{2-x}$ system (M_0, saturated magnetic moment; $\vec{k}$, magnetic propagation vector; $*$, values calculated from parameters indicated in last column, †, present work, lattice constants at room temperature).

x	Struct.	a [Å]	c [Å]	T_C [K]	T_N [K]	M_0 [μ_B]	$\vec{k}$ [r.l.u]	Ref.
2.0	$MgCu_2$	7.794		14(1)		7.9(1)‖[111]	(0, 0, 0)	[1, 2]
1.75	$MgCu_2$	7.778		14(1)		$4.83|_{T=9K}$‖[111]	(0, 0, 0)	[5, 9, 15]
				10.5(2)		$7.9(1)|_{T=1.5K}$‖[111]	(0, 0, 0)	[25], †
				17.7*		8.45*‖[111]		B_n^m, H_{mf}
1.0	AlB_2	4.425	3.515		2.8(3)	$4.9(1)|_{T=1.4K}$ ⊥ [001]	$(\frac{1}{3}, \frac{1}{3}, 0.472)$	[5, 9, 15]
					5.9(1)	4.59* ⊥ [001]		B_n^m, T_N
0.5	AlB_2	4.371	3.581		2.5(3)	$3.8(1)|_{T=1.4K}$ ⊥ [001]	$(\frac{1}{3}, \frac{1}{3}, 0.451)$	[5, 9, 15]
					3.2(1)	4.17* ⊥ [001]		B_n^m, T_N

In this paper we present inelastic neutron scattering experiments on the pseudo-ternary system $ErAl_xGa_{2-x}$ for $x = 0.5$, 1.0 and 1.75 in order to determine its CEF. Thermodynamic

properties reconstructed from the obtained CEF parameters are compared with neutron diffraction measurements of the magnetic moment and with macroscopic measurements of the specific heat and the magnetic susceptibility. Conclusions on the electronic properties of the system with different Ga concentration are drawn.

2. Experiment

Polycrystalline samples of $ErAl_xGa_{2-x}$ ($x = 0.5$, 1.0, 1.75) were prepared according to the method described previously in [5, 15], i.e. by arc-melting the starting elements ($\geqslant$99.9% purity) under argon atmosphere. Analysis by x-ray and neutron diffraction revealed single phases for all three samples. In contrast to earlier work [5, 15] (i.e. figure 1) no admixture of the intermediate-c/a AlB_2 or the $CeCu_2$ phases could be observed for the $ErAl_{0.5}Ga_{1.5}$ sample. Hence it is considered to be in the same phase as ErAlGa.

The neutron inelastic scattering measurements (INS) were performed on the cold triple-axis spectrometer DrüchaL at the SINQ spallation source in Villigen, Switzerland with vertically focusing monochromator and horizontally focusing analyser. The energy-loss configuration was chosen with a fixed analyser energy of $E_f = 4.9$ meV and fixed scattering vectors $Q = 1.0$, 1.2, 1.6 and 2.1 Å^{-1}. Higher-order contamination was suppressed by using a cooled Be filter after the sample. The samples were ground to fine powders and under He atmosphere sealed into cylindrical Al containers of 9 mm diameter (total sample volume $\approx$3 cm^3). For cooling a closed-cycle He refrigerator was used except for the $ErAl_{1.75}Ga_{0.25}$ sample, which was measured in a standard ILL cryostat. The neutron diffraction measurements of $ErAl_{1.75}Ga_{0.25}$ were performed on the powder diffractometer DMC at SINQ with a neutron wavelength of $\lambda = 2.56$ Å. Measurements of the magnetic susceptibility and the specific heat were carried out using an induction magnetometer and a Quantum Design PPMS system, respectively.

3. Theoretical background

3.1. Crystal field and molecular field

The splitting of the $2J + 1 = 16$-fold degenerate ground state J-multiplet of the Er^{3+} ion is a direct consequence of the quantum mechanical Stark effect caused by the electric field of its neighbouring ions (crystal field). Hence the point symmetry at the Er^{3+} site determines the exact splitting scheme of the ground-state J-multiplet. Neglecting admixtures of higher J-multiplets the electric potential leading to the CEF can be conveniently expressed using the Stevens operator equivalents $\hat{O}_n^m$, which are functions of the angular momentum operators $\hat{J}_z$, $\hat{J}^+$ and $\hat{J}^-$ [16]. In the cubic $ErAl_2$ and $ErAl_{1.75}Ga_{0.25}$ the Er^{3+} occupies a site of cubic $\bar{4}3m$ symmetry. The interaction of the f electrons with the CEF potential can be written with the Hamiltonian [17]

$$\hat{H}_{cef}^{cub} = B_4(\hat{O}_4^0 + 5\hat{O}_4^4) + B_6(\hat{O}_6^0 - 21\hat{O}_6^4) \tag{1}$$

where B_4 and B_6 are the CEF parameters. The ground state J-multiplet is split by $\hat{H}_{cef}^{cub}$ into three quartet states ($3\Gamma_8$) and two doublet states (Γ_6, Γ_7) (figure 2) [18]. For the hexagonal ErAlGa and $ErAl_{0.5}Ga_{1.5}$ compounds the Er^{3+} occupies a site of $6/mmm$ symmetry, so that the crystal-field Hamiltonian is given by [17]

$$\hat{H}_{cef}^{hex} = B_2^0\hat{O}_2^0 + B_4^0\hat{O}_4^0 + B_6^0\hat{O}_6^0 + B_6^6\hat{O}_6^6 \tag{2}$$

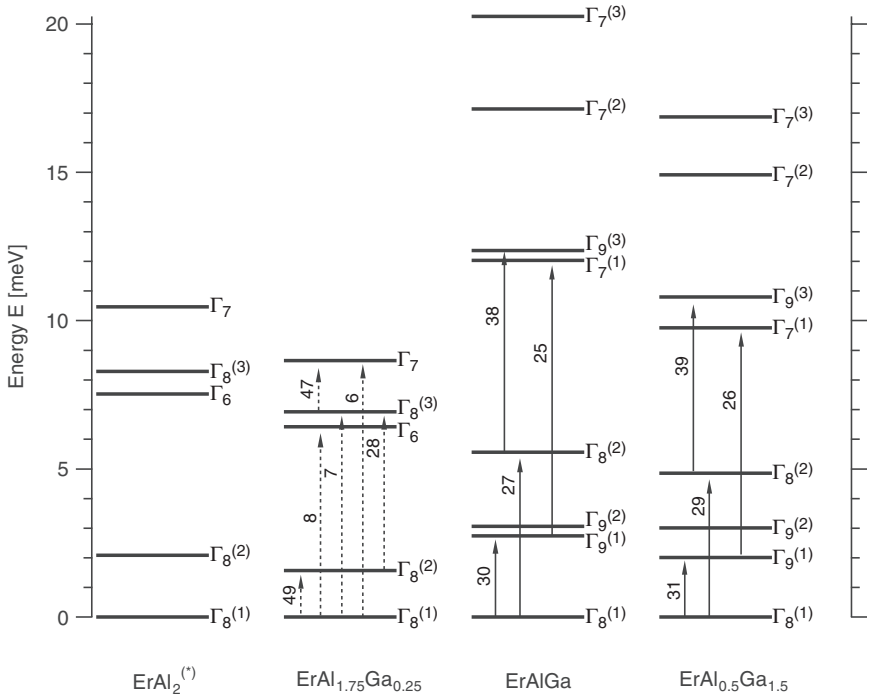

Figure 2. CEF level scheme of $ErAl_xGa_{2-x}$ resulting from parameters *final* listed in table 2. Arrows denote observed energy transitions, dashed arrows indicate observed but unresolved transitions. Numbers on arrows give the relative strength of the corresponding transition-matrix elements. (*) $ErAl_2$ after [2].

resulting in eight Kramers doublets ($3\Gamma_7, 2\Gamma_8, 3\Gamma_9$) (figure 2) [19]. Below the magnetic ordering temperature the rare-earth ion is also subject to the internal magnetic field, which can be described in the mean-field approximation by

$$\hat{H}_{mf} = -g^2\mu_B^2\lambda\langle\hat{\vec{J}}\rangle\hat{\vec{J}} \tag{3}$$

with the angular momentum $\vec{J}$ and the Landé factor g of the rare-earth ion, a molecular-field parameter λ and the Bohr magneton μ_B. In equation (3) the non-operator term $\sim O(\langle\hat{\vec{J}}\rangle^2)$ is omitted as it only causes a shift in the energy scale. The $2J + 1$ eigenvectors $|n\rangle$ of the Hamiltonian $\hat{H} = \hat{H}_{cef} + \hat{H}_{mf}$ define all experimental observables. For a system of N non-interacting rare-earth ions the neutron cross-section for the CEF transition $|\Gamma_n\rangle \rightarrow |\Gamma_m\rangle$ in the dipole approximation is given by

$$\frac{\mathrm{d}^2\sigma}{\mathrm{d}\Omega\,\mathrm{d}\omega} = N\left(\frac{\gamma e^2}{m_e c^2}\right)\frac{k_1}{k_0}\mathrm{e}^{-2W(\vec{Q})}F^2(\vec{Q})p_n|\langle\Gamma_m|\hat{J}_\perp|\Gamma_n\rangle|^2\delta(E_n - E_m + \hbar\omega) \tag{4}$$

where k_0, k_1 denote the wave numbers for the incoming and scattered neutron, respectively, $\hbar\omega$ the energy transfer of the neutron, $W(\vec{Q})$ the Debye–Waller factor, $F(\vec{Q})$ the magnetic form factor, $p_n = p_n(T)$ the Boltzmann factor for state $|\Gamma_n\rangle$ and $J_\perp$ the operator of the total angular momentum's component perpendicular to the scattering vector $\vec{Q}$. All remaining symbols have their usual meaning.

Table 2. Crystal-field parameters (Stevens) obtained by least-squares fits to the observed INS spectra ($ErAl_2$ after [1], all values in meV). For ErAlGa and $ErAl_{0.5}Ga_{1.5}$ two CEF sets are given. The easy axis of magnetization at room temperature favours the first set labelled *final*. Note that the sign of B_6^6 remains undetermined in $6/mmm$ point-symmetry [17].

$MgCu_2$ type	$B_4 \times 10^3$	$B_6 \times 10^5$	H_{mf} [kOe]	$\lambda_{mf} \times 10^2$ [meV]	
$ErAl_2$	0.110	−0.134			
$ErAl_{1.75}Ga_{0.25}$	0.102(20)	−0.111(6)	75(7)	7.9(7)	
AlB_2 type	set	$B_2^0 \times 10^2$	$B_4^0 \times 10^4$	$B_6^0 \times 10^5$	$\pm B_6^6 \times 10^4$
ErAlGa	*final*	−0.38(16)	0.36(12)	−0.698(13)	0.159(13)
	alternative	0.05	0.50	−0.689	0.161
$ErAl_{0.5}Ga_{1.5}$	*final*	−0.51(27)	0.66(17)	−0.588(26)	0.122(14)
	alternative	0.49	0.97	−0.566	0.128

3.2. Extended point-charge model

In principle the CEF parameters can be calculated on the basis of the structural parameters and the charges of the ions, i.e. by the point-charge model (PCM). Generally the CEF parameters can then be expressed (in Stevens notation) by

$$B_n^m = A_n^m \langle r^n \rangle \chi_n \gamma_n^m \tag{5}$$

with reduced CEF parameters A_n^m reflecting the charge distribution independent of geometry and rare earth, $\langle r^n \rangle$ the nth radial moment of the 4f electron and χ_n the Stevens coefficients and geometric coordination factors γ_n^m calculated by the PCM. Morrison [20] has introduced an extension of the original PCM, which corrects the free Hartree–Fock 4f radial moments $\langle r^n \rangle \to \langle r^n \rangle / \tau^n$ for the situation of ions embedded in solids and which takes into account the shielding due to the outer $5s^2$ and $5p^6$ shells of the rare-earth ion by scaling $B_n^m \to (1-\sigma_n) B_n^m$. τ and σ_n are phenomenological parameters of the rare-earth ion tabulated in [20]. In the case of metals the conduction electrons further screen the CEF potential. In the Thomas–Fermi theory of screening (strictly valid in the free-electron approximation only) this effect is implemented by substituting the Coulomb potential by a screened Coulomb potential (i.e. the Yukawa potential) with a screening factor k_0 proportional to the square root of the density of states at the Fermi level $D(E_F)$ [21, 22]. Even with these extensions the PCM generally fails to predict the parameters quantitatively for metallic compounds. However it has proven to be helpful in order to account for general tendencies and dependencies of the CEF parameters upon a change in chemical structure or upon the substitution of ions.

Below we will use the PCM in the context of metals assuming strong screening. It is hence valid to consider the electric potential caused by nearest neighbours of the rare-earth only. In this limit the effect of the conduction electrons can be discussed equally well by either introducing a screening parameter k_0 or by reducing the effective charge of the ligand and thus decreasing the reduced CEF parameters A_n^m. E.g. in cubic symmetry with lattice constant a one finds [23]

$$\tilde{A}_n(k_0) = A_n(0) \left(1 - \frac{k_0^2 a^2}{\eta_n} \right) \qquad \eta_4 = 14, \eta_6 = 22 \tag{6}$$

with $A_n(0)$ the unscreened reduced CEF parameter.

4. Results and data analysis

4.1. $ErAl_{1.75}Ga_{0.25}$

The measured INS spectra of $ErAl_{1.75}Ga_{0.25}$ for temperatures above and below the magnetic ordering temperature $T_C = 10.5$ K are shown in figure 3. In the paramagnetic state the spectrum shows some unresolved inelastic intensity near the elastic line and a broad bump around 6 meV. Based on these experimental data no unambiguous set of CEF parameters can be found. Hence we also performed measurements in the ordered state, where the additional splitting of the CEF levels into separate singlet states due to the molecular field serves as a crucial check for the corresponding eigenfunctions. According to earlier work [1, 2, 15] the direction of the magnetic moments is along $\langle 111 \rangle$. Based on the Hamiltonians equation (1) and equation (3) a self-consistent least-squares procedure yielded the CEF parameters B_4 and B_6 and the molecular field $\vec{H}_{mf} = \lambda g \mu_B \langle \vec{J} \rangle$. The resulting parameters are listed in table 2. The molecular field $\vec{H}_{mf}$ accounts for $T_C \approx 17.7$ K—higher than actually observed—and a saturated moment of $M_0 \equiv M(T \to 0) = 8.45\ \mu_B$.

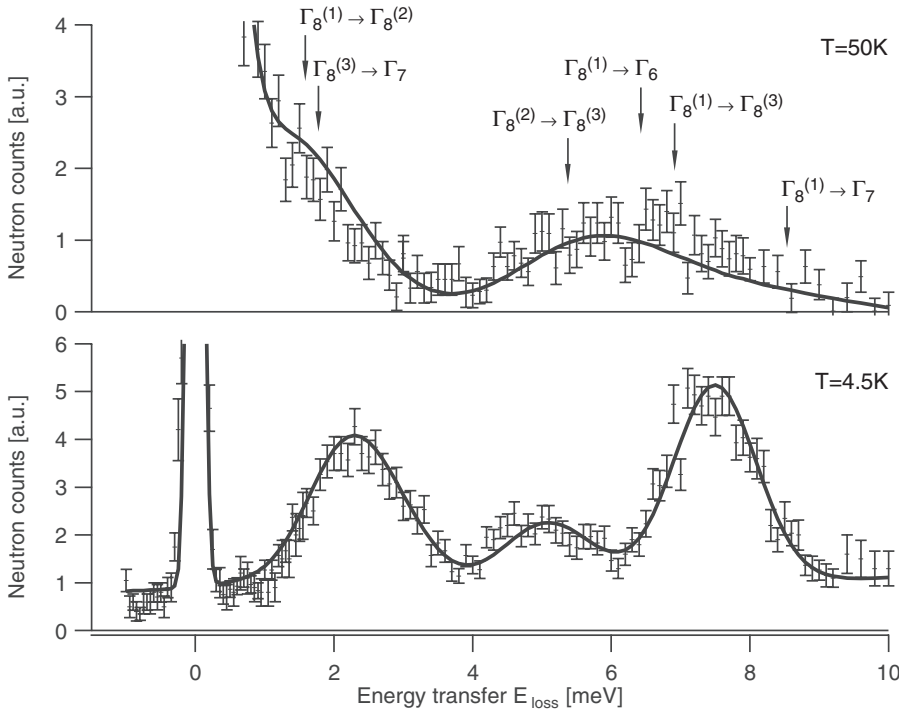

Figure 3. INS spectra for $ErAl_{1.75}Ga_{0.25}$ in the paramagnetic ($T = 50$ K) and in the Zeeman split state ($T = 4.5$ K) with $E_f = 4.9$ meV, $Q = 1.0$ and 1.6 Å^{-1} (corrected for magnetic form factor, background subtracted, height of the elastic line is around 29 counts for $T = 4.5$ K). The curve is the result of the least-squares fit procedure as explained in the text.

In order to check the CEF parameters we have carried out additional specific heat and neutron diffraction measurements. Both resulted in $T_C = 10.5(1)$ K in contrast to $T_C = 14$ K published in earlier work [9, 15]. The Rietveld refinement of the diffraction data yielded a magnetic moment of $M = 7.9(1)\ \mu_B$ at $T = 1.5$ K. However regarding the mean-field approach as being the simplest way to incorporate magnetic order, we may well accept T_C and M_0

reconstructed from the CEF. Figure 4 shows the dependence of the reduced magnetic moment on reduced temperature obtained from the neutron diffraction measurement in comparison with the CEF calculation. The agreement is satisfactory. The obtained CEF parameters also account well for the [111] axis being the easy magnetic axis up to room temperature. The values found for $ErAl_{1.75}Ga_{0.25}$ are close to those of $ErAl_2$ [1, 2]: they match within 7% for B_4 and 20% for B_6. However they follow an opposite trend to smaller values as the lattice constant a is reduced in contrast to equation (5), where $\gamma_n^m \propto a^{-(n+1)}$ holds. Hence the partial substitution with Ga ions is likely to change the electronic properties of the solid too.

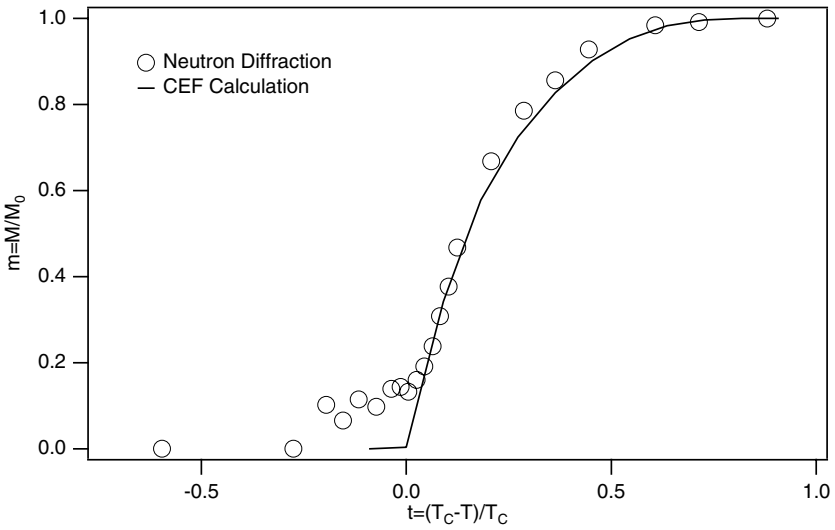

Figure 4. Reduced magnetic moment versus reduced temperature for $ErAl_{1.75}Ga_{0.25}$ (open symbols by neutron diffraction, solid line by reconstruction with the obtained CEF parameters). The moment above T_C is most likely caused by fluctuations and concentration inhomogeneities in the compound.

4.2. ErAlGa

The neutron spectra for ErAlGa are shown in figure 5. At $T = 15$ K two broad peaks can be observed. At higher temperature $T = 50$ K the peak around 6 meV develops a shoulder at the right side and a new weak peak around 9 meV appears. The magnetic origin of the peaks is established by noting that the dependence of their intensity with momentum transfer Q follows the form factor $F(Q)$ in equation (4). Obviously the two additional features at $T = 50$ K result from CEF transitions from excited states that are not sufficiently populated at $T = 15$ K. All peaks are distinctly broader than the instrumental resolution ($\Gamma_{inst}(\Delta E = 0\,\text{meV}) \approx 0.22\,\text{meV}$, $\Gamma_{inst}(\Delta E = 6\,\text{meV}) \approx 0.42\,\text{meV}$). A least-squares fit on equation (2) resulted in two CEF sets both describing the observed neutron spectra equally well (table 2), i.e. resulting in the same energy splitting and transition-matrix elements except for one of the eight Kramers doublets, namely $\Gamma_9^{(2)}$. However no strong INS transition from or to the $\Gamma_9^{(2)}$ state can be observed in either set. In figure 5 the solid line indicates the fit by the first set of parameters given in table 2 to which also the energy-level scheme of figure 2 and labelling in figure 5 refer. On the basis of other experimental methods presented below, we are going to show that in analogy to $ErAl_{0.5}Ga_{1.5}$ this CEF set is the favoured one.

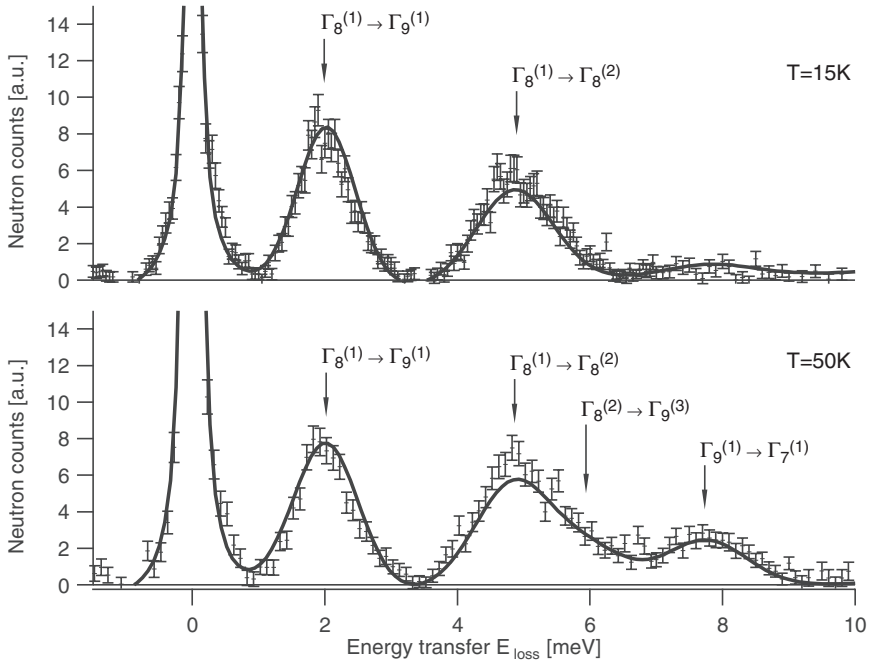

Figure 5. INS spectra for ErAlGa with $E_f = 4.9$ meV, $Q = 1.2$ and 1.6 Å^{-1} (corrected for magnetic form factor, background subtracted, height of the elastic line is around 24 counts). The curve denotes the least-squares fit by CEF parameters *final* given in table 2.

4.3. $ErAl_{0.5}Ga_{1.5}$

The neutron spectra of $ErAl_{0.5}Ga_{1.5}$ show the same characteristics as for ErAlGa with a smaller overall splitting (figure 6). The data were fitted using the same procedure as for the ErAlGa sample and similarly resulted in two possible CEF sets as listed in table 2. For both samples the two sets differ by the sign of the second-order CEF parameter B_2^0. It has been shown in [24] that the second-order term of the $1/T$ expansion of the magnetic susceptibility (or the constant term in the inverse susceptibility) depends only on the second-order CEF and on the bilinear exchange and thus entirely governs the magnetic anisotropy in the high-temperature limit. Indeed a mean-field calculation of the magnetic susceptibility shows that for the $ErAl_{0.5}Ga_{1.5}$ sample the two CEF sets yield different easy axes at temperatures $T > 20$ K (figure 7), whereas for the ErAlGa sample the easy axis is oriented along [001] for both CEF sets. Hence the determination of the easy axis of $ErAl_{0.5}Ga_{1.5}$ at elevated temperatures serves as a crucial check for the CEF parameters.

We prepared grain-aligned samples of $ErAl_{0.5}Ga_{1.5}$ and ErAlGa by mixing well grained powder with epoxy resin. The resin was filled in Torlon cylinders of 6 mm diameter and hardened at room temperature in a magnetic field of 9 T perpendicular to the cylinder axis. Slices of the cylinders were then analysed on a single-crystal neutron diffractometer and on an induction magnetometer. The chosen geometry allowed us to measure the susceptibility without correcting for shape anisotropy. Both samples exhibited pronounced preferred orientation along the c-axis coinciding with the direction of the magnetic field used for the alignment. This allowed us to conclude that in $ErAl_{0.5}Ga_{1.5}$ the first CEF set with the c-axis being the easy axis at room temperature must be preferred ($B_0^2 < 0$).

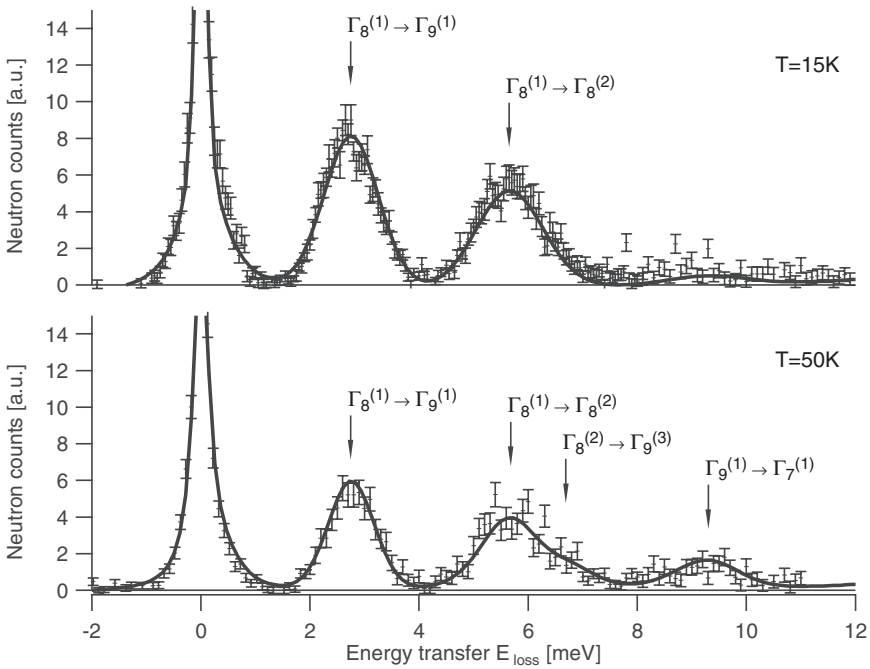

Figure 6. INS spectra for $ErAl_{0.5}Ga_{1.5}$ with $E_f = 4.9$ meV, $Q = 1.3$, 1.6 and 2.1 Å^{-1} (corrected for magnetic form factor, background subtracted, height of the elastic line is around 27 and 50 counts, respectively). The curve denotes the least-squares fit by CEF parameters *final* given in table 2.

Finally the close analogy in the geometry and in the sequence of energy levels between ErAlGa and $ErAl_{0.5}Ga_{1.5}$ suggests the first CEF set with $B_2^0 < 0$ being favoured in ErAlGa too.

5. Discussion

Pseudo-ternary compounds allow us to study systematically the dependence of the CEF potential upon partial substitution of the ligands. The increase of Ga concentration in RAl_xGa_{2-x} affects the CEF firstly, as it induces a change in geometry and secondly, because the electronic properties of the solid are modified. $ErAl_{1.75}Ga_{0.25}$ has a slightly smaller lattice constant than $ErAl_2$; nevertheless it shows a smaller overall CEF splitting of only about 8.5 meV compared to about 10.5 meV of $ErAl_2$ (figure 2) in spite of equation (5). In order to understand this effect we have performed calculations based on the extended point-charge model introduced in section 3.1. Assuming a strong screening due to the conduction electrons only the closest shell of neighbouring ions around the rare-earth ion has been considered in order to calculate the coordination factors γ_n^m of equation (5). Specifically for the cubic case only the four closest rare-earth neighbours have been considered (the similarly distanced, spherically arranged 12 surrounding Al/Ga ions lead to small γ_n^m only), for the hexagonal case the 12 nearest Al/Ga ions plus the two close apex rare-earth ions have been considered. In the reduction of the CEF parameters the corrections by Morrison have been taken into account. Table 3 lists the reduced CEF parameters A_n^m of $ErAl_xGa_{2-x}$ together with CEF parameters for R = Nd and Ho taken from [10, 11] and reduced by the same procedure. Except for

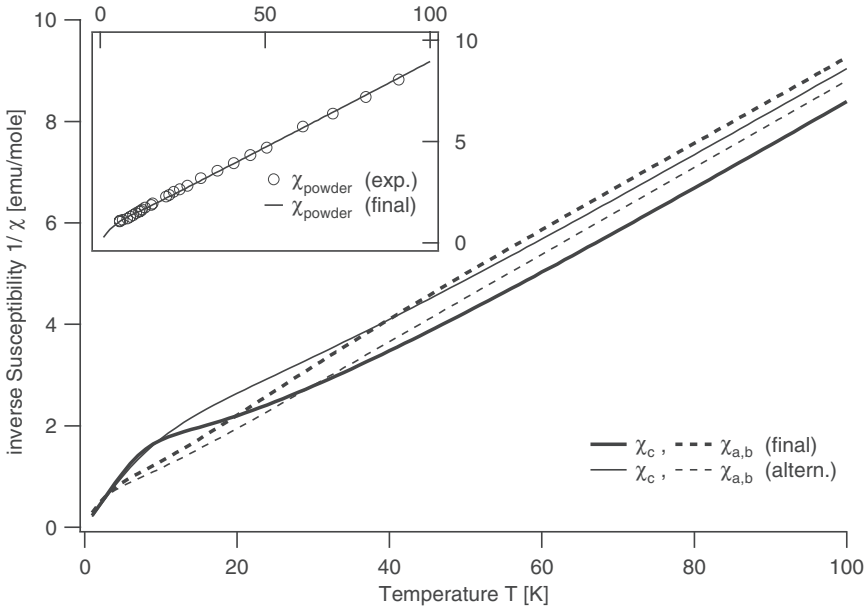

Figure 7. Calculated inverse magnetic susceptibility $1/\chi$ for the two CEF sets of $ErAl_{0.5}Ga_{1.5}$. Only the *final* set leads to the c-axis being the easy direction of magnetization for $T > 20$ K in accordance with the results obtained for the grain-aligned sample. The inset compares the measurements on powder with the powder-averaged calculation.

A_2^0, for which the approximation of considering only nearest neighbour ions is too poor, the values of all reduced CEF parameters are very close together and show the same tendency to lower absolute values upon an increase of the Ga concentration. As pure geometric effects are cancelled out by the reduction of the CEF parameters, the large decline of the CEF potential upon Ga-increase directly reflects the change in the electronic properties of these systems. According to equation (6) our model may ascribe this effect to a reduction of the effective charge of the ligands ($\propto A_n^m \downarrow$) or to an increase of the screening ($k_0 \uparrow$). Assuming a linear relationship between the free-electron concentration n and Ga content $y \equiv 2 - x$ one expects for the functional dependence of A_n^m on y in free-electron approximation (equation (6) with $k_0^2 \propto D(E_F) \propto n^{1/3} \propto (y + y_0)^{1/3}$)

$$A_n(k_0) = A_n(0)(1 - \alpha_n(y + y_0)^{1/3}) \tag{7}$$

with proportionality factor α and offset constant y_0. A fit of the most dominant and experimentally best determined parameter A_6^0 on equation (7) is shown in figure 8 for $ErAl_xGa_{2-x}$ and supports this simple model qualitatively.

In the INS spectra the experimentally observed linewidth of the $\Gamma_8^{(1)} \rightarrow \Gamma_9^{(1)}$ and $\Gamma_8^{(1)} \rightarrow \Gamma_8^{(2)}$ transitions are about 1.1 meV and 1.3 meV, respectively (figures 5 and 6). Hence they are clearly broader than the instrumental resolution that only accounts for about 0.3 meV and 0.4 meV, respectively. Magnetic dispersion effects contribute to less than 0.6 meV to the line broadening at $T = 15$ K as can be roughly estimated by a random-phase-approximation calculation (assuming eight nearest rare-earth neighbours with equal exchange constants). However concentration inhomogeneities within these pseudo-ternary compounds of macroscopic Al concentration $0 \leqslant x \leqslant 2$ may well explain the observed broadening. Namely, considering only the $N = 12$ next-nearest group-III ions around

Table 3. Reduced CEF parameters A_n^m found in the RAl_xGa_{2-x} family with Morrison's corrections applied (all values in units of [10^4 meV Å], M = Al/Ga, (*) these compounds crystallize in the AlB_2 structure with intermediate c/a-ratio where the two rare-earth apex ions have not been considered for coordination).

	Coord.	A_2^0	A_4^0	A_6^0	$\pm A_6^6$	Ref.
$ErAl_2$	4R		−1.20	−5.34		[1]
$ErAl_{1.75}Ga_{0.25}$	4R		−1.10	−4.34		Present work
ErAlGa	12M + 2R	−0.043	−0.113	−3.63	1.15	Present work
$ErAl_{0.5}Ga_{1.5}$	12M + 2R	−0.051	−0.195	−3.37	0.918	Present work
$HoAl_2$	4R		−1.22	−4.14		[1]
HoAlGa	12M + 2R	0.030	−0.249	−3.00	1.40	[10]
$NdAl_2$	4R		−1.25	−5.90		[1, 11]
$NdAl_{1.25}Ga_{0.75}$	12M + 2R	0.025	−0.261	−4.45	1.58	[11]
NdAlGa*	12M	−0.052	−0.103	−2.12	2.02	[11]
$NdAl_{0.5}Ga_{1.5}$ *	12M	−0.043	−0.099	−1.29	1.45	[11]
$NdGa_2$ *	12M	−0.025	−0.056	−0.356	0.628	[11]

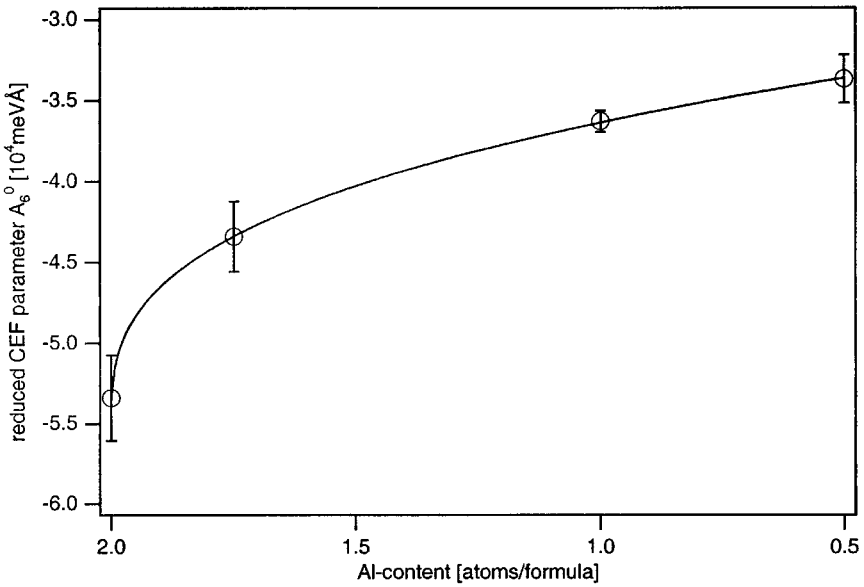

Figure 8. Functional dependence of the reduced CEF parameter A_6^0 on the Al/Ga content in $ErAl_xGa_{2-x}$. With increasing Ga concentration the CEF potential becomes more screened. The solid line is a fit to equation (7) as described in the text.

the Er^{3+} ion, which can be either occupied by Al or Ga, we end up with 13 distinct configurations having $0 \leqslant m \leqslant 12$ Al ions. These configurations are binomially distributed with probabilities $p_m(x) = \binom{N}{m}(x/2)^m(1 - x/2)^{N-m}$ and local Al content $\tilde{x} = 2m/N$ ($0 \leqslant \tilde{x} \leqslant 2$). Extrapolating linearly the CEF parameters for the 13 distinct configurations with local Al content $\tilde{x}$ from the CEF parameters found for ErAlGa and $ErAl_{0.5}Ga_{1.5}$, we can estimate their respective energy-level schemes. Adding up all configurations according to their probabilities p_m we end up with total linewidths $\Gamma = 1.1$ meV and 1.4 meV for the two transitions in ErAlGa and $\Gamma = 1.0$ meV and 1.2 meV in $ErAl_{0.5}Ga_{1.5}$, respectively, in

close agreement with the experimental linewidths. Evidence for microscopic concentration inhomogeneities in the $ErAl_xGa_{2-x}$ system are also found in macroscopic properties: firstly, the magnetic moment in $ErAl_{1.75}Ga_{0.25}$ shows a pronounced tail above the ordering temperature (figure 4), secondly, measurements of the specific heat in $ErAl_{1.75}Ga_{0.25}$ and ErAlGa feature broad transition peaks [25] and thirdly, the chemical phase diagram hosts large regions of phase coexistence (figure 1).

6. Conclusions

By means of inelastic neutron scattering we have established the CEF splitting in $ErAl_xGa_{2-x}$ for three different Al concentrations $x = 1.75, 1.0, 0.5$ which crystallize in two distinct structural phases. Within the same chemical structure the observed change in the CEF upon the increase of the Ga content cannot be solely attributed to the change in lattice dimensions. Point-charge model calculations suppose a modification in the electronic properties of the solid upon the addition of Ga ions resulting in an increase of the electron concentration. This finding is in accord with the observed structural phase transitions common to many members of the RAl_xGa_{2-x} family. The change from the cubic $MgCu_2$ Laves phase to the hexagonal AlB_2 follows the general sequence $MgCu_2$–$MgZn_2$–$ThSi_2$ found for many of the MN_2 phases upon the increase of the electron concentration [26]. However in the rare-earth compounds (M = R) only the $MgCu_2$ and the AlB_2 structure are realized, the latter being in close relation to the $MgZn_2$ structure. The isostructural phase transition within the AlB_2 phase upon further increase of the Ga concentration also cannot be explained on geometric arguments only. On the basis of well established near-neighbour diagrams of the AlB_2 structure [12] the difference in atomic radii of Al and Ga [27], though in sign correct, proves to be too small in order to cause the change in c/a (i.e. the transition). However for intermetallic MN_2 phases with the AlB_2 structure Pearson [13] has shown that depending on the valence of the M atom the reduced strain parameter is shifted resulting in two distinct families of MN_2 phases with different c/a-ratios. Although Al and Ga correspond to the same group in the periodic system the increase of Ga concentration obviously influences the electronic properties of the solid. Further experimental evidence for an increase of the electron concentration is found from the following arguments: firstly, the lattice constant a decreases with Ga in agreement with Pauling's empirical equation (e.g. in [12]) applied on the bond lengths of the B atoms (B–B $= \sqrt{3}a$ in AlB_2) implying an increased valence electron concentration (VEC) for the Ga-rich compounds. Secondly, $ErGa_2$ shows a larger electric conductivity than $ErAl_2$ [28, 29]. Hence we conclude that the observed structural phase transitions are electronically driven by a Hume–Rothery-like mechanism rather than by mere geometric factors. Further investigations of the pressure dependence upon the structure of RAl_xGa_{2-x} compounds are under way to elucidate the exact mechanism responsible for the different structures found in these pseudo-ternary systems.

Acknowledgments

The authors are grateful to Dr O E Martin for the sample preparation, to Drs M Mali and J Roos of the preparation of the grain aligned samples and to Dr E Clementyev for valuable discussions. We thank Drs L Keller and J Schefer for the help on the diffractometers DMC and TriCS.

References

[1] Purwins H G and Leson A 1990 *Adv. Phys.* **39** 309

[2] Purwins H G, Walker E, Barbara B, Rossignol M F and Furrer A 1976 *J. Phys. C: Solid State Phys.* **9** 1025
[3] Moze O 1998 *Handbook of Magnetic Materials* vol 11, ed K H J Buschow (Amsterdam: Elsevier) pp 493ff
[4] Dwight A E 1968 *Proc. 7th Rare Earth Res. Conf. (Coronado)* vol 1, p 273
[5] Martin O E and Girgis K 1983 *J. Magn. Magn. Mater.* **37** 228
[6] Girgis K and Fischer P 1979 *J. Physique Coll.* **40** (suppl 5) C5 159
[7] Beck L and Girgis K 1985 *J. Less-Common. Met.* **109** 275
[8] Talik E, Heimann J and Chelkowski A 1986 *J. Less-Common. Met.* **123** L13
[9] Martin O E, Girgis K and Fischer P 1983 *J. Magn. Magn. Mater.* **37** 231
[10] Ball A R, Gignoux D, Schmitt D and Zhang F Y 1993 *Phys. Rev.* B **47** 11 887
[11] Furrer A and Martin O E 1986 *J. Phys. C: Solid State Phys.* **19** 3863
[12] Pearson W B 1972 *The Crystal Chemistry and Physics of Metals and Alloys* (New York: Wiley–Interscience)
[13] Pearson W B 1979 *Proc. R. Soc.* A **365** 523
[14] Brunner G O 1977 *Acta Crystallogr.* A **33** 226
[15] Martin O E 1982 *PhD Thesis* 7132 Eidgenössische Technische Hochschule Zürich
[16] Hutchings M T 1965 *Solid State Phys.* **16** 227
[17] Walter U 1984 *J. Phys. Chem. Solids* **45** 401
[18] Lea K R, Leask M J M and Wolf W P 1962 *J. Phys. Chem. Solids* **23** 1381
[19] Segal E and Wallace W E 1970 *J. Solid State Chem.* **2** 347
[20] Morrison C A 1988 *Angular Momentum Theory Applied to Interactions in Solids* (Berlin: Springer) p 111
[21] Ashcroft N W and Mermin N D 1976 *Solid State Physics* (Fort Worth: Saunders College Publishing)
[22] Mesot J 1995 *Magnetic Neutron Scattering* ed A Furrer (Singapore: World Scientific) p 178
[23] Tellenbach U 1974 *Diploma Thesis* AF-SSP-76 Delegation für Ausbildung und Hochschulforschung am Eidg. Institut für Reaktorforschung, Würenlingen
[24] Boutron P 1972 *Phys. Rev.* B **7** 3226
[25] Strässle Th 1999 *Diploma Thesis* LNS-200 Eidgenössische Technische Hochschule Zürich
[26] Raman A 1967 *Z. Metallkde.* **58** 179
[27] Teatum E, Gschneidner K and Waber J 1960 *LA*-2345 US Department of Commerce, Washington, DC
[28] van Daal H J and Buschow K H J 1969 *Solid State Commun.* **7** 217
[29] Blanco J A *et al* 1992 *J. Magn. Magn. Mater.* **104–107** 1285